To be published in OSA Continuum:

Title: Mid-infrared diffraction-free space-time wave packets

Authors: Murat Yessenov,Qitian Ru,Kenneth Schepler,Monjurul Meem,Rajesh Menon,Konstantin Vodopyanov,Ayman Abouraddy

Accepted: 01 February 20

Posted 01 February 20

DOI: https://doi.org/10.1364/OSAC.384544

Mid-infrared diffraction-free space-time wave packets

Murat Yessenov[1,*], Qitian Ru[1], Kenneth L. Schepler[1], Monjurul Meem[2], Rajesh Menon[2], Konstantin L. Vodopyanov[1], and Ayman F. Abouraddy[1]

[1] *CREOL, The College of Optics & Photnics, University of Central Florida, Orlando, FL 32816, USA*
[2] *Department of Electrical & Computer Engineering, University of Utah, Salt Lake City, UT 84112, USA*
[*] *yessenov@knights.ucf.edu*

Abstract: Joint structuring of the spatio-temporal spectrum of a pulsed optical beam can lead to a host of unusual properties, such as diffraction-free propagation and tunable group velocities in free space. Such 'space-time' wave packets have been synthesized exclusively in the visible and near-infrared spectral regions. Here we synthesize the first space-time wave packet in the mid-infrared exploiting a transmissive phase plate fabricated via gray-scale lithography. A mid-infrared wave packet having a bandwidth of $\sim$ 60 nm at a wavelength of 2.35 μm is synthesized such that its transverse width is $\sim$ 300 μm, and is monitored for a propagation distance of 7 m, corresponding to 80$\times$ the Rayleigh range of a Gaussian beam at the same wavelength having the same width. The experimental methodology presented here and the reported results will help appropriate spatio-temporally structured light in the mid-infrared for a wide variety of applications including imaging, sensing, and metrology.

1. Introduction

Mid-infrared (MIR) radiation (1.5 – 5 μm) is of interest for a plethora of applications [1], driven primarily by the fact that many molecular species have strong characteristic vibrational transitions in this spectral region. Consequently, MIR sensing is useful for trace-gas detection and can thus help monitor industrial and natural emissions in a number of industries [2]. Additionally, MIR light is of great interest for medical diagnostics [3] (e.g., breath analysis [4]), for remote detection of harmful chemicals [5], and for infrared countermeasures against heat-seeking missiles [6]. Many of these applications require beam transmission over extended distances to small target regions, which opens a need for non-diffracting MIR beams. However, the large bandwidths typically utilized in applications of MIR light add an additional constraint on the realization of diffraction-free beams, so that simple spatial structuring of the field does not suffice and joint spatio-temporal structuring is instead necessary. Indeed, although extensive work has been carried out in the visible and near-infrared spectral regions regarding beam shaping and ultrafast pulse modulation, much less work has been performed in the MIR. Examples include temporal structuring of MIR laser pulses [7, 8] and spatial structuring of monochromatic MIR beams [9–11].

Recently, a family of spatio-temporally structured pulsed beams termed 'space-timeâĂŹ (ST) wave packets have been synthesized in the near-infrared, which have several unique properties that can also be useful for MIR applications. For instance, ST wave packets propagate rigidly in free space without diffraction or dispersion [12]; ST wave packets self-heal after traversing opaque obstacles [13]; they have been demonstrated to propagate for extended distances [14, 15]; and they can propagate at arbitrary group velocities in free space [16] and transparent optical materials [17, 18]. Such wave packets have had a long history from early proposals [19, 20] to the synthesis of instances of ST wave packets [21–23]; see [24–28] for reviews. Our recent

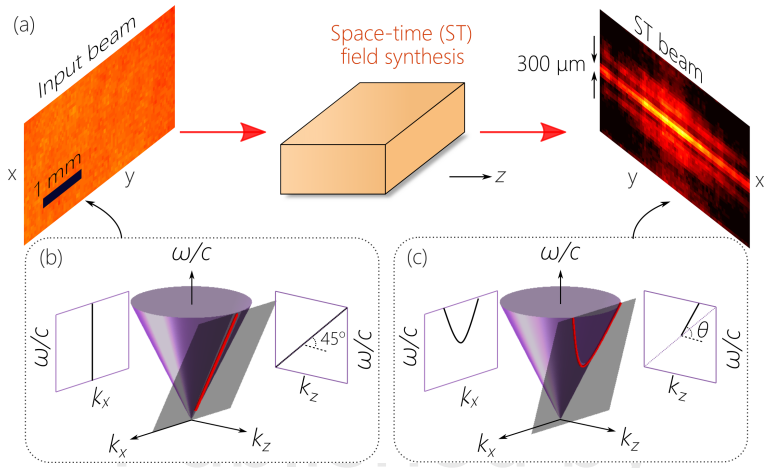

Fig. 1. Concept of space-time wave packets. (a) A plane-wave pulse having uniform intensity profile (left) undergoes spatio-temporal spectral phase modulation to produce a ST wave packet having the form of a light-sheet (right). The intensity profiles are both measured. (b) Spectral representation of a plane-wave pulse on the surface of the light-cone in $(k_x, k_z, \frac{\omega}{c})$-space, corresponding to the field on the left in (a). The spatio-temporal locus lies along the tangent to the light-cone at $k_x = 0$. (c) Spectral representation of a ST wave packet on the surface of the light-cone in $(k_x, k_z, \frac{\omega}{c})$-space, corresponding to the field on the right in (a). The spatio-temporal locus is again one-dimensional, but now lies at the intersection of the light-cone with a tilted spectral plane.

success with producing ST wave packets has been facilitated by a novel synthesis approach based on spectral-phase modulation performed jointly in space and time [29]. Independently, several recent theoretical studies have appeared that are introducing new concepts into this field [30–35].

The unique properties of ST wave packets stem from distinct underlying spatio-temporal correlations introduced into the wave packet spectrum that can also be implemented in principle in the MIR. However, to the best of our knowledge, there have been no previous reports on the synthesis of spatio-temporal structuring of MIR wave packets.

Here we present the first demonstration of a ST wave packet synthesized in the MIR via spatio-temporal spectral phase modulation. Because spatial light modulators that operate in the MIR are lacking, we make use instead of transmissive phase plates [36] fabricated via gray-scale lithography. The synthesized MIR field is in the form of a light-sheet having a central beam width of ~ 300 μm and bandwidth of ~ 60 nm at a wavelength of 2.35 μm that propagates for a distance of 7 m distance, corresponding to 80× the Rayleigh range of a Gaussian beam of the same transverse width and at the same wavelength. This work paves the way to utilization in the MIR of the properties of ST wave packets that have been previously verified in the visible and near-infrared, for applications ranging from remote-sensing and stand-off detection to novel nonlinear phase-matching schemes.

2. Concept of diffraction-free space-time wave packets

ST wave packets are a class of pulsed beams endowed with a distinct feature: each spatial frequency k_x (transverse component of the wave vector) underlying the spatial profile is tightly associated with a particular wavelength λ (or temporal frequency ω), in contrast to traditional wave packets where the spatial and temporal spectra are typically independent of each other. The concept of ST wave packets is therefore best described in the Fourier space $(k_x, k_z, \frac{\omega}{c})$,

where k_z is the longitudinal component of the wave vector along the axial dimension z, and c is the speed of light in vacuum. In this spectral domain, the free-space dispersion relationship $k_x^2 + k_z^2 = (\frac{\omega}{c})^2$ can be represented geometrically by a cone, referred to hereon as the 'light-cone'. Any monochromatic plane wave corresponds to a point $(k_x, k_z, \frac{\omega}{c})$ on the light-cone. Consequently, the spatio-temporal spectrum of a *monochromatic* beam lies along the intersection of the light-cone with the horizontal *iso*-frequency plane $\omega = \omega_o$. Such a field has a finite spatial bandwidth but no temporal bandwidth. As a second example, the spectrum of a *plane-wave pulse* lies along the tangent of the light-cone with respect to a plane that is parallel to the k_x-axis and therefore tilted at an angle $\theta = 45°$ with respect to the k_z-axis. Such a field has a finite temporal bandwidth but no spatial bandwidth. A conventional *pulsed beam* (or wave packet) having both finite spatial *and* temporal bandwidths is thus represented by a two-dimensional patch on the surface of the light-one, and the spatio-temporal spectrum is typically separable with respect to the spatial and temporal frequencies k_x and ω, respectively [37].

Contrary to traditional wave packets, the spectrum of a ST wave packet traces a *one*-dimensional trajectory on the surface of the light-cone rather than a *two*-dimensional patch; that is, the spatio-temporal spectrum is *not* separable with respect to k_x and ω, and the reduced-dimensionality of the spectrum can thus be viewed as a manifestation of classical entanglement [38], which is *the* central characteristic shared by all propagation-invariant wave packets [19–21, 26, 28, 37]. The spectral representation of propagation-invariant ST wave packets take the form of conic sections resulting from the intersection of the light-cone with a spectral plane that is parallel to the k_x-axis and tilted by an angle θ with respect to the k_z-axis. Such a plane is thus represented by the equation $\omega - \omega_o = (k_z - k_o)c \tan\theta$, where ω_o is a fixed frequency and $k_o = \frac{\omega_o}{c}$ is the corresponding wave number, so that the spectral plane passes through the point $(0, k_o, k_o)$ on the light-cone. We refer to θ as the spectral tilt angle, and it should be emphasized that it is not a physical angle, rather an internal degree of freedom of the wave packet. The projection of the spatio-temporal spectrum onto the $(k_z, \frac{\omega}{c})$-plane is a straight line, indicating that the group velocity of this wave packet in free space is dictated solely by the spectral tilt angle $v_g = \frac{\partial\omega}{\partial k_z} = c \tan\theta$ [16].

A second critical internal degree of freedom of ST wave packets is the *spectral uncertainty* $\delta\omega$, which is the unavoidable fuzziness in the association between spatial and temporal frequencies. The ideal case described above in which each k_x is associated precisely with a single ω in fact corresponds to an infinite-energy wave packet. Finite-energy ST wave packets are thus characterized by a finite spectral uncertainty $\delta\lambda$ that sets the limit on the maximal propagation distance [38] and differential group delay [39] achievable.

3. Experimental method

3.1. Infrared laser beam

We have recently introduced a novel linear phase-only approach for spectral synthesis of ST wave packets [12, 29]. The procedure starts with a plane-wave pulse [Fig. 1(b)] directed to a spatio-temporal synthesis arrangement [Fig. 1(a)] that introduces the required space-time correlations into the field. The resulting field is endowed with a one-to-one correlation between the spatial and temporal frequencies (modulo the sign of the spatial frequency $\pm k_x$), which guarantees the propagation invariance of the resulting ST wave packet [Fig. 1(c)]. The overall layout of our synthesis system is shown schematically in Fig. 2.

The infrared laser source of the input pulses used in this work is a Kerr-lens mode locked Cr^{2+}:ZnS laser pumped by a continuous wave erbium-doped fiber laser [40]. This laser delivers pulses of width 62 fs and bandwidth ~ 90 nm centered at a wavelength of 2.35 μm and repetition rate of 79 MHz. The laser beam has ~ 1.2-W average power and is linearly polarized in the horizontal direction. The measured spectrum of the laser is shown in Fig. 3(a). Before entering the ST synthesis arrangement, the beam is expanded by a telescope system consisting of two

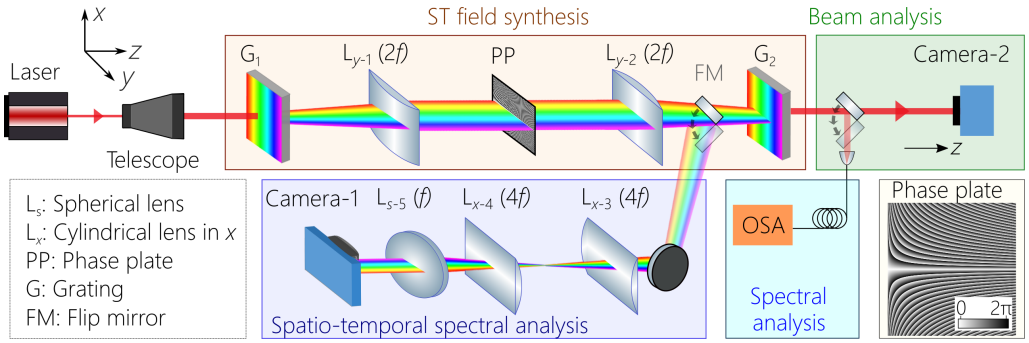

Fig. 2. Schematic of the optical setup for synthesis and characterization of ST wave packets, consisting of four major sections: (i) A field synthesis section that introduces the spatio-temporal correlations into the input field, thereby producing MIR diffraction-free ST wave packets. (ii) Spatio-temporal spectral analysis section to characterize the ST beam in Fourier space (k_x,λ). (iii) Beam analysis section to observe the ST field in physical space by capturing the transverse time-averaged intensity along the propagation axis z. (iv) Spectral analysis of ST wave packets. For consistency with our previous work, the direction vertical to the optical table is denoted as the x-axis; consequently, the horizontal direction is the y-axis. In the bottom right corner we plot the two-dimensional phase distribution implemented on the phase plate.

lenses: an aspherical ZnSe lens with focal length $f = 25$ mm (25-mm-diameter) and a spherical BK-7 lens of focal length $f = 316$ mm (50-mm-diameter), thereby expanding the beam from an initial size of 1.5 mm to a final size of 19 mm [Fig. 1(a)]. This expanded beam approximates the plane-wave pulse to be used as the input for ST wave packet synthesis.

3.2. *Spatio-temporal spectral synthesis*

The experimental setup for generating MIR ST wave-packets depicted in Fig. 2 is similar to our previously demonstrated layout utilized in the near-infrared at a wavelength of ~ 800 nm [12,36,41], and in general combines techniques that are well-known in ultrafast pulse shaping [42] and beam shape modulation [43].

The incident plane-wave pulse from the laser source (see previous sub-section) is directed to a reflective diffraction grating G_1 (Newport 53004BK01-570R, 26×26 mm^2, 600 lines/mm), which in combination with a cylindrical lens L_{y-1} ($f = 200$ mm) spreads the spectrum along the y-axis (horizontal). A transmissive phase plate inscribed by gray-scale lithography [44] (see below) is placed at the Fourier plane of L_{y-1}. This phase plate is designed to imprint a linear phase distribution along the x-axis (vertical) to be associated with the wavelength λ incident at that location of the phase plate (the spectrum is spread along the horizontal y-axis). The linear phase corresponds is that associated with a plane-wave having a spatial frequency k_x, thus establishing the desired assignment of k_x to $\lambda(k_x)$. Another cylindrical lens L_{y-2} (identical to L_{y-1}) and diffraction grating G_2 (identical to G_1) recombine the spatially resolved spectrum and reconstitute the pulse. The optical field emerging from the grating G_2 is endowed with the required spatio-temporal correlations that guarantee diffraction-free and dispersion-free behavior thereafter.

3.3. *Phase plate design and fabrication*

In this experiment we make use of a phase plate to impress a two-dimensional phase distribution on the spectrally-resolved optical field in order to introduce the desired spatio-temporal correlations – rather than use a spatial light modulator (SLM) as in our previous work. Although SLMs have an

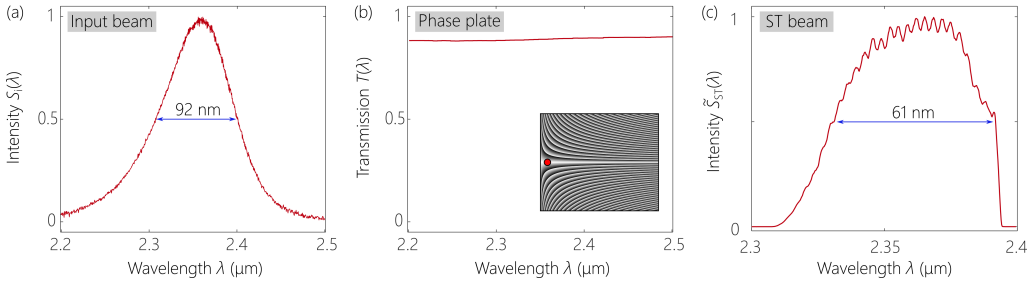

Fig. 3. (a) Measured spectrum of the input beam from the Cr^{2+}:ZnS laser with $\Delta\lambda \approx 90$ nm. (b) Measured transmission spectrum of the phase plate in the wavelength range of interest. The inset shoes the location on the phase plate where the transmission measurement was performed. (c) Measured spectrum of the synthesized MIR ST wave packet.

obvious advantage with respect to dynamically varying the implemented phase distribution, they nevertheless have a limited spectral operation range that excludes to date the MIR, in addition to their low-energy handling capability. Therefore, to synthesize MIR ST wave packets we exploit a phase plate fabricated via gray-scale lithography. The designed phase profile ϕ for the plate was first converted into a topographical height pattern h through the transformation $h = \frac{\lambda}{2\pi} \cdot \frac{\phi}{n-1}$, where λ is the illumination wavelength and n is the refractive index of the mask material at λ. A minimum feature width of 3 μm, maximum feature height of 2.6 μm, and 100 height-level discretizations are achievable with our fabrication process. The mask itself was fabricated using gray-scale optical lithography in the photopolymer S1813 (Microchem). By adjusting the exposure dose (based upon a previous calibration step), one can generate precise discrete height levels in the photopolymer after development.

The fabrication process starts with a 2.6-μm-thick film of positive-tone photoresist (Shipley 1813). The photopolymer was spun at 1000 rpm for 60 s on a 2-inch-diameter, 0.6-mm-thick D263 soda lime glass wafer as a support substrate. The sample was then baked in an oven at 110 °C for 30 minutes. A calibration was conducted to determine the depth of the photoresist after development for a given exposure dose as described previously [44, 45], then a laser pattern generator (Heidelberg Instruments) was used to write the design. The exposed sample was then developed in AZ 1 : 1 solution for 35 s followed by DI water rinse and then dried with nitrogen. The 0.6-mm-thick soda-lime glass wafer has high optical transmission for wavelengths shorter than 2.4 μm as seen in Fig. 3(b). The measured spectral transmittance over the range $2.2 - 2.5$ μm includes Fresnel reflection from the phase plate interfaces and the absorption in the phase plate material, but remains close to $\sim 90\%$ over the spectral range of interest. For longer wavelengths, a different substrate such as sapphire or silicon can be used.

A phase plate was produced with this method having an active area of 25×20 mm^2 and was designed to accommodate 60 nm bandwidth centered at a wavelength of 2.35 μm. Wavelengths from the input beam that lie outside of this spectrum are filtered out by means of an opaque cover around the active area of the phase plate. A plot of the phase pattern inscribed on the phase plate is given in Fig.2 (bottom right corner).

3.4. Characterization

The resulting ST wave packets are analyzed in two different measurement modalities: (1) Fourier-space analysis; and (2) beam profiling of the ST wave packet in physical space along the propagation axis.

First, the beam is characterized in Fourier space (k_x, λ) to ensure that the desired spatio-

temporal spectral correlations are indeed achieved. By sampling the spectrally resolved field before the grating G_2 and implementing a spatial Fourier transform via the spherical lens L_{s-5} ($f = 75$ mm) in a $2-f$ configuration, we resolve the field in (k_x, λ) space at the focal plane of the lens, where it is captured by a pyroelectric camera (Camera-1; Pyrocam III, 12.4×12.4-mm^2 active area, 85-μm-sized pixels separated by 100 μm). To improve the quality of the captured spatio-temporal spectrum on the camera, we first de-magnify the field before the lens L_{s-5} along the x-axis (vertical) via a $4-f$ system of cylindrical lenses L_{x-4} ($f = 500$ mm) and L_{x-5} ($f = 100$ mm). The demagnification in physical space results in a magnification in Fourier space along k_x.

Second, to test the non-diffracting behavior of the ST wave packet, we scan another pyroelectric camera (Camera-2; Pyrocam III) along the propagation axis z, and capture the time-averaged intensity $I(x, y)$ at different positions along the z-axis. Here the origin of the z-axis is taken to be the location of the last grating G_2, where the pulse is reconstituted and the ST wave packet is generated.

4. Results

4.1. Measurements of the spatio-temporal spectrum

In this experiment the phase plate is designed to synthesize infrared ST wave packets with a spectral tilt angle of $\theta = 45.005°$ having a bandwidth of $\Delta\lambda \sim 60$ nm (from the initial ~ 90-nm-bandwidth pulses). The spectrum of the synthesized ST wave packet is plotted in Fig. 3(c). The spectrum is measured by focusing the beam with a silver-coated parabolic reflective collimator into a single mode ZrF_4 fiber (core diameter of 9 μm, NA = 0.19) coupled to an optical spectrum analyzer (OSA; Yokogawa, model AQ6376).

The association between the spatial frequencies k_x and the assigned wavelength λ introduced by means of the phase plate is confirmed by measuring the spatio-temporal spectrum $|\widetilde{\psi}(k_x, \lambda)|^2$, which is plotted in Fig.4(a). For $\theta = 45.005°$, the intersection of the spectral plane with the light-cone takes the form of a hyperbola [37]. However, because the bandwidth used is narrow with respect to the central wavelength, the measured segment of the hyperbola is well-approximated by a parabola [16–18]. The measured data in Fig. 4(a) is in excellent agreement with the

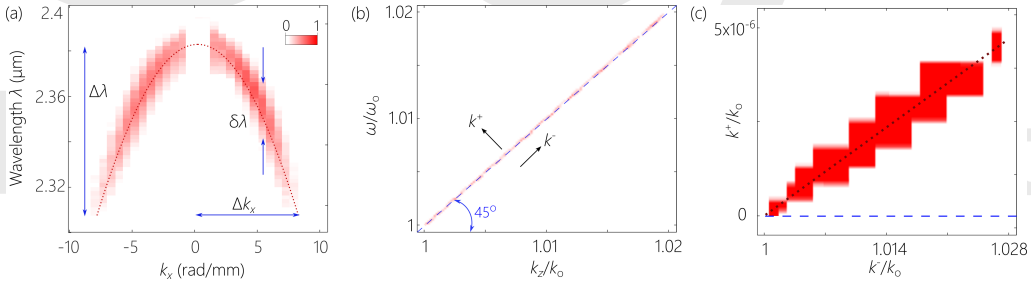

Fig. 4. (a) Spatio-temporal spectral intensity $|\tilde{\psi}(k_x, \lambda)|^2$ measured by Camera-1, where $\delta\lambda \approx 150$ pm, $\Delta\lambda \approx 60$ nm, $\Delta k_x \approx 8$ rad/mm and the red dotted line corresponds to a theoretical plot of the spatio-temporal spectral trajectory of the ST wave packet when $\theta = 45.005°$. (b) The measured spatio-temporal spectral intensity plot projected onto the $(k_z, \frac{\omega}{c})$-plane. The blue dashed line represents the light line $k_z = \frac{\omega}{c}$. Because of the very small deviation between the spectral tilt angle $\theta = 45.005°$ and the light-line (tilted at 45°), they appear to coincide. (c) Same plot as (b) but in a rotated coordinate system (k^+, k^-) to bring out the deviation of the spatio-temporal spectrum from the light-line (dashed blue line). The dark-red dotted line corresponds to the theoretical expectations.

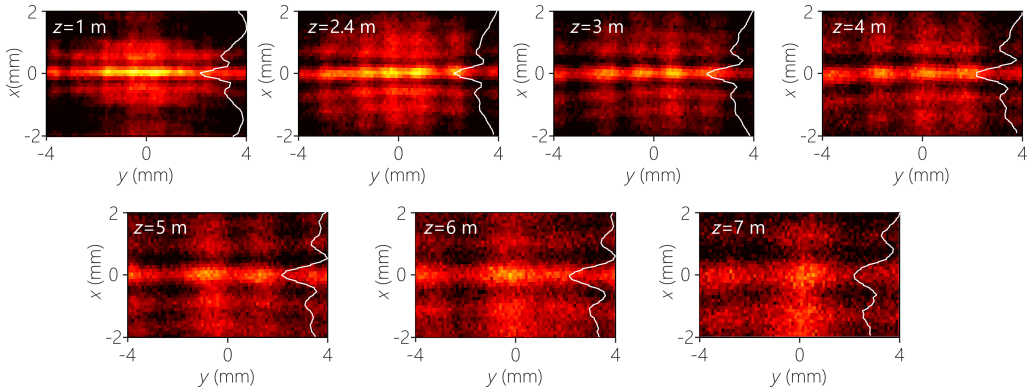

Fig. 5. Measured time-averaged transverse intensity profiles $I(x, y)$ of the ST wave packet along the propagation direction at axial positions $z \approx 1$, 2.4, 3, 4, 5, 6, and 7 meters.

theoretically expected parabolic trajectory (red dotted line in the plot). The fuzziness in the measured spatio-temporal spectrum is a consequence of the the pyroelectric camera limitations (pixel size and noise threshold), and thus the estimate of the spectral uncertainty $\delta\lambda$ obtained from this measurement is likely to significantly exceed the actual value.

Further confirmation that the implemented spectral tilt angle is indeed $\theta = 45.005°$ is obtained by plotting the measured spatio-temporal spectrum projected onto the $(k_z, \frac{\omega}{c})$-plane [Fig.4(b)]. This projection takes the form of a line, which signifies that the pulse propagates in free space without dispersion at a group velocity slightly above the speed of light c, $v_g = c \tan\theta = 1.0002c$. To identify the deviation of the plotted spatio-temporal trajectory $|\widetilde{\psi}(k_z, \frac{\omega}{c})|^2$ as depicted in Fig.4(b) from the light-line (blue dashed line, corresponding to $\theta = 45°$, we re-plot the data for the spatio-temporal spectrum in a rotated coordinate basis (k^+, k^-), which is rotated counter-clockwise by an angle 45° with respect to the $(k_z, \frac{\omega}{c})$ basis [Fig.4(c)]. From this plot we see clearly that the slope of the spectral trajectory is indeed the targeted value for the spectral tilt angle. Note once again the impact of the pixelation of the pyroelectric camera leading to an exaggeration in the spectral uncertainty.

4.2. *Axial evolution of the ST wave packet*

The time-averaged transverse intensity profile $I(x, y)$ is captured at multiple axial locations from $z = 1$ m to $z = 7$ m along the propagation axis by Camera-2 [Fig. 2], and the measurements are shown in Fig. 5. The intensity distribution is uniform along the y-axis where it retains the size of the initially expanded wave front, whereas the field is finely structured along the x-axis. Along the x-axis, the beam transverse profile has a width of $\Delta x \sim 300\mu$m, as expected from the spatial bandwidth of $\Delta k_x = 8$ rad/mm introduced in the synthesis arrangement [Fig. 3(a)]. By monitoring the propagation of the beam over a distance of 7‘m, we note that these fine features are not lost, despite this distance being $\sim 80 \times z_R$, where z_R is the Rayleigh range of a Gaussian beam of spatial width 300 μm at a wavelength of 2.35 μm.

We have previously shown [15,39] that the maximum propagation distance of ST wave-packets is *not* dictated by the beam size or the pulse width, instead it is determined by only the internal degrees of freedom of the St wave packet [29]: the spectral tilt angle θ and the spectral uncertainty $\delta\omega$. The maximum propagation distance L_{max} (defined as the distance after which the on-axis intensity drops to half its initial value) is related to θ and $\delta\omega$ through the equation:

$$L_{max} \sim \frac{c}{\delta\omega} \frac{1}{|1 - \cot\theta|}. \tag{1}$$

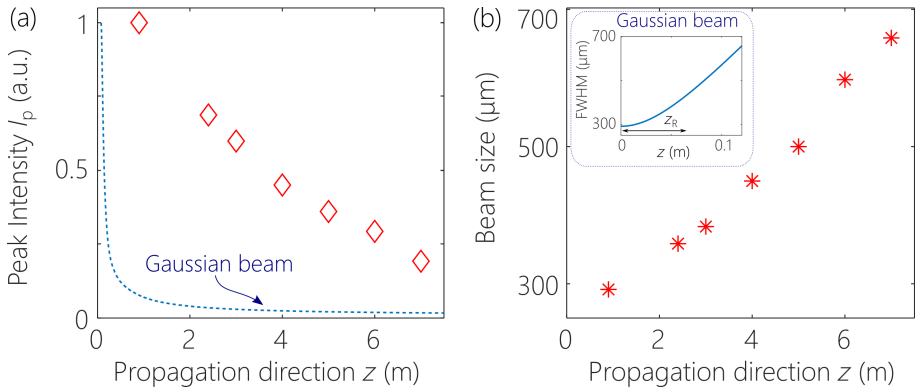

Fig. 6. (a) Measured normalized on-axis peak intensity $I_p(x = 0, z)$ with propagation distance z. The data is compared to the decay of a Gaussian beam (dotted curve) of the same width and at the same wavelength. (b) Change in beam width (FWHM) with propagation distance z. Inset shows the increase in width for the corresponding Gaussian beam.

Using a diffraction grating of 600 lines/mm and 26-mm-width results in a spectral uncertainty of $\delta\omega \approx 5 \times 10^{10}$ rad/s. Consequently, with this estimated value of $\delta\omega$ and the confirmed value of θ, we expect a maximum propagation distance in the range $L_{\max} \sim 10 - 30$ m.

In Fig.6(a) we plot the measured on-axis peak intensity $I_{\rm p}(x=0, z)$, and in Fig. 6(b) we plot the beam size Δx along the propagation axis z. The peak intensity of the infrared ST wave packet drops to 20% of its initial value after a distance of $z = 7$ m, whereas the peak intensity of a Gaussian beam having the same initial width drops to the same amount at $z = 0.3$ m. Similarly, the beam width of the ST wave packet doubles upon propagation for a distance of $L_{\max} = 7$ m distance, a distance that corresponds to $L_{\max}/z_{\rm R} \sim 80$ with respect to a Gaussian beam having the same initial width.

5. Discussion and Conclusion

We have presented the first example of MIR spatio-temporally structured wave packets in which elements of ultrafast pulse modulation and beam shaping are combined to produce diffraction-free pulsed beams. We synthesized a 60-nm-bandwidth pulse at a wavelength of 2.35 μm in which each wavelength is associated with one spatial frequency, resulting in a 300-μm-wide spatial profile maintained for a propagation distance of 7 m, which is $\sim 80\times$ the Rayleigh range of a corresponding Gaussian beam. Such demonstrations have been carried out in the visible and near-infrared by utilizing SLMs to implement the requisite spectral-phase modulation. Because such SLMs are lacking in the MIR, we designed and fabricated a transmissive phase plate [36] that introduces the target phase modulation at the high level of precision necessary for the synthesis of ST wave packets. We expect that this work will initiate further investigations concerning the generation of MIR ST wave packets and their potential applications.

Finally, we note that the unique features of coherent ST wave packets are maintained when utilizing incoherent optical fields for their synthesis [41, 46]. Specifically, the diffraction-free behavior is retained when the precise spatio-temporal correlations introduced in the case of coherent wave packets are used with an incoherent light source [41], and the spectral tilt angle controls the ‘coherence group velocityâĂŹ, which is the speed of the peak of the cross-correlation function of the incoherent ST field with respect to the initial incoherent source [46]. We expect that these two features can be realized with incoherent MIR fields, where thermal (incoherent) fields are particularly useful in imaging, radiometry, and metrology.

Funding

Office of Naval Research (ONR) (N00014-17-1-2458, N66001-10-1-4065, N00014-15-1-2659); Defense Advanced Research Projects Agency (DARPA) (W31P4Q-15-1-0008).

Acknowledgments

We are grateful to IPG Photonics–Mid-infrared Lasers for providing the mode-locked Cr:ZnS laser. We thank Yertay Zhiyenbayev for assistance in the experiment and Abbas Shiri for useful discussions.

Disclosures

The authors declare no conflicts of interest.

References

1. F. K. Tittel, D. Richter, and A. Fried, *Mid-Infrared Laser Applications in Spectroscopy* (Springer, Berlin, Heidelberg, 2003), vol. 89 of *Topics in Applied Physics*.
2. Z. Du, S. Zhang, J. Li, N. Gao, and K. Tong, "Mid-infrared tunable laser-based broadband fingerprint absorption spectroscopy for trace gas sensing: A review," Appl. Sci. **9**, 338 (2019).
3. V. Serebryakov, E. BoÄŋko, N. Petrishchev, and A. Yan, "Medical applications of mid-ir lasers. problems and prospects," J. Opt. Technol. **77**, 6–17 (2010).
4. B. Henderson, A. Khodabakhsh, M. Metsälä, I. Ventrillard, F. M. Schmidt, D. Romanini, G. A. D. Ritchie, S. te Lintel Hekkert, R. Briot, T. Risby, N. Marczin, F. J. M. Harren, and S. M. Cristescu, "Laser spectroscopy for breath analysis: towards clinical implementation," Appl. Phys. B **124**, 161 (2018).
5. R. Bogue, "Remote chemical sensing: a review of techniques and recent developments," Sens. Rev. **38**, 453–457 (2018).
6. G. Overton, "Photonics applied: Defense: IR countermeasures aim for safer flights," LaserFocusWorld **47** (2011).
7. D. B. Strasfeld, S.-H. Shim, and M. T. Zanni, "New advances in mid-ir pulse shaping and its application to 2d ir spectroscopy and ground-state coherent control," Adv. Chem. Phys. **141**, 1 (2009).
8. P. Krogen, H. Suchowski, H. Liang, N. Flemens, K.-H. Hong, F. X. Kärtner, and J. Moses, "Generation and multi-octave shaping of mid-infrared intense single-cycle pulses," Nat. Photonics **11**, 222 (2017).
9. J. Tao, B. Meng, B. Hu, G. Z. Liang, and Q. J. Wang, "Mid-infrared bessel beams generation by subwavelength structure on quantum cascade laser," in *2012 Photonics Global Conference (PGC),* (IEEE, 2012), pp. 1–3.
10. A. Aadhi, V. Sharma, R. P. Singh, and G. K. Samanta, "Continuous-wave, singly resonant parametric oscillator-based mid-infrared optical vortex source," Opt. Lett. **42**, 3674–3677 (2017).
11. A. Camper, H. Park, Y. H. Lai, H. Kageyama, S. Li, B. K. Talbert, C. I. Blaga, P. Agostini, T. Ruchon, and L. F. DiMauro, "Tunable mid-infrared source of light carrying orbital angular momentum in the femtosecond regime," Opt. Lett. **42**, 3769–3772 (2017).
12. H. E. Kondakci and A. F. Abouraddy, "Diffraction-free space-time beams," Nat. Photon. **11**, 733–740 (2017).
13. H. E. Kondakci and A. F. Abouraddy, "Self-healing of space-time light sheets," Opt. Lett. **43**, 3830–3833 (2018).
14. B. Bhaduri, M. Yessenov, and A. F. Abouraddy, "Meters-long propagation of diffraction-free space-time light sheets," Opt. Express **26**, 20111–20121 (2018).
15. B. Bhaduri, M. Yessenov, D. Reyes, J. Pena, M. Meem, S. R. Fairchild, R. Menon, M. C. Richardson, and A. F. Abouraddy, "Broadband space-time wave packets propagating for 70 m," Opt. Lett. **44**, 2073–2076 (2019).
16. H. E. Kondakci and A. F. Abouraddy, "Optical space-time wave packets of arbitrary group velocity in free space," Nat. Commun. **10**, 929 (2019).
17. B. Bhaduri, M. Yessenov, and A. F. Abouraddy, "Space-time wave packets that travel in optical materials at the speed of light in vacuum," Optica **6**, 139–146 (2019).
18. B. Bhaduri, M. Yessenov, and A. F. Abouraddy, "Anomalous refraction of optical space-time wave packets," unpublished (2019).
19. J. N. Brittingham, "Focus wave modes in homogeneous Maxwell's equations: Transverse electric mode," J. Appl. Phys. **54**, 1179–1189 (1983).
20. J.-Y. Lu and J. F. Greenleaf, "Nondiffracting X waves – exact solutions to free-space scalar wave equation and their finite aperture realizations," IEEE Trans. Ultrason. Ferroelec. Freq. Control. **39**, 19–31 (1992).
21. P. Saari and K. Reivelt, "Evidence of X-shaped propagation-invariant localized light waves," Phys. Rev. Lett. **79**, 4135–4138 (1997).
22. K. Reivelt and P. Saari, "Experimental demonstration of realizability of optical focus wave modes," Phys. Rev. E **66**, 056611 (2002).
23. D. Faccio, A. Averchi, A. Couairon, M. Kolesik, J. Moloney, A. Dubietis, G. Tamosauskas, P. Polesana, A. Piskarskas, and P. D. Trapani, "Spatio-temporal reshaping and X wave dynamics in optical filaments," Opt. Express **15**, 13077–13095 (2007).

24. K. Reivelt and P. Saari, "Localized wave solutions of the scalar homogeneous wave equation and their optical implementation," arxiv:physics/0309079 (2003).
25. A. P. Kiselev, "Localized light waves: Paraxial and exact solutions of the wave equation (a review)," Opt. Spectrosc. **102**, 603–622 (2007).
26. H. E. Hernández-Figueroa, E. Recami, and M. Zamboni-Rached, eds., *Localized waves* (Wiley-Interscience, 2008).
27. J. Turunen and A. T. Friberg, "Propagation-invariant optical fields," Prog. Opt. **54**, 1–88 (2010).
28. H. E. Hernández-Figueroa, E. Recami, and M. Zamboni-Rached, eds., *Non-diffracting Waves* (Wiley-VCH, 2014).
29. M. Yessenov, B. Bhaduri, H. E. Kondakci, and A. F. Abouraddy, "Weaving the rainbow: Space-time optical wave packets," Opt. Photon. News **30**, 34–41 (2019).
30. M. A. Porras, "Gaussian beams diffracting in time," Opt. Lett. **42**, 4679–4682 (2017).
31. N. K. Efremidis, "Spatiotemporal diffraction-free pulsed beams in free-space of the Airy and Bessel type," Opt. Lett. **42**, 5038–5041 (2017).
32. L. J. Wong and I. Kaminer, "Abruptly focusing and defocusing needles of light and closed-form electromagnetic wavepackets," ACS Photon. **4**, 1131–1137 (2017).
33. L. J. Wong and I. Kaminer, "Ultrashort tilted-pulsefront pulses and nonparaxial tilted-phase-front beams," ACS Photon. **4**, 2257–2264 (2017).
34. P. Saari, "Reexamination of group velocities of structured light pulses," Phys. Rev. A **97**, 063824 (2018).
35. P. Saari, O. Rebane, and I. Besieris, "Reexamination of energy flow velocities of non-diffracting localized waves," Phys. Rev. A **100**, 013849 (2019).
36. H. E. Kondakci, M. Yessenov, M. Meem, D. Reyes, D. Thul, S. R. Fairchild, M. Richardson, R. Menon, and A. F. Abouraddy, "Synthesizing broadband propagation-invariant space-time wave packets using transmissive phase plates," Opt. Express **26**, 13628–13638 (2018).
37. M. Yessenov, B. Bhaduri, H. E. Kondakci, and A. F. Abouraddy, "Classification of propagation-invariant space-time light-sheets in free space: Theory and experiments," Phys. Rev. A **99**, 023856 (2019).
38. H. E. Kondakci, M. A. Alonso, and A. F. Abouraddy, "Classical entanglement underpins the propagation invariance of space-time wave packets," arXiv:1812.10566 (2018).
39. M. Yessenov, B. Bhaduri, L. Mach, D. Mardani, H. E. Kondakci, M. A. Alonso, G. A. Atia, and A. F. Abouraddy, "What is the maximum differential group delay achievable by a space-time wave packet in free space?" Opt. Express **27**, 12443–12457 (2019).
40. S. B. Mirov, V. V. Fedorov, D. Martyshkin, I. S. Moskalev, M. Mirov, and S. Vasilyev, "Progress in mid-IR lasers based on Cr and Fe-doped IIâĂŞVI chalcogenides," IEEE J. Sel. Top. Quantum Electron. **21**, 292–310 (2015).
41. M. Yessenov, B. Bhaduri, H. E. Kondakci, M. Meem, R. Menon, and A. F. Abouraddy, "Non-diffracting broadband incoherent space-time fields," Optica **6**, 598–607 (2019).
42. A. M. Weiner, *Ultrafast Optics* (John Wiley & Sons, Inc., 2009).
43. C. Maurer, A. Jesacher, S. Bernet, and M. Ritsch-Marte, "What spatial light modulators can do for optical microscopy," Laser Photon. Rev. **5**, 81–101 (2011).
44. N. Mohammad, M. Meem, X. Wan, and R. Menon, "Full-color, large area, transmissive holograms enabled by multi-level diffractive optics," Sci. Rep. **7**, 5789 (2017).
45. P. Wang, J. A. Dominguez-Caballero, D. J. Friedman, and R. Menon, "A new class of multi-bandgap high-efficiency photovoltaics enabled by broadband diffractive optics," Prog. Photovolt. **23**, 1073–1079 (2015).
46. M. Yessenov and A. F. Abouraddy, "Changing the speed of optical coherence in free space," Opt. Lett. **44**, 5125–5128 (2019).